minerals

MDPI

Article

Valentinite and Colloform Sphalerite in Epithermal Deposits from Baia Mare Area, Eastern Carpathians

Gheorghe Damian [1,2], Andrei Buzatu [2], Ionut Andrei Apopei [2,*], Zsolt László Szakács [1], Ioan Denuț [1,3], Gheorghe Iepure [1] and Daniel Bârgăoanu [2]

1 North University Centre of Baia Mare, Technical University of Cluj-Napoca, 430083 Baia Mare, Romania; gdamian_geo@yahoo.com (G.D.); szakacsz@yahoo.com (Z.L.S.); ioan.denut@gmail.com (I.D.); iepureg@yahoo.com (G.I.)

2 Department of Geology, Faculty of Geography and Geology, "Alexandru Ioan Cuza" University of Iași, 700505 Iași, Romania; andrei.buzatu@uaic.ro (A.B.); birgaoanu.daniel@yahoo.com (D.B.)

3 County Museum of Mineralogy, "Victor Gorduza", 430212 Baia Mare, Romania

* Correspondence: andrei.apopei@uaic.ro

Received: 9 December 2019; Accepted: 26 January 2020; Published: 30 January 2020

Abstract: Valentinite forms through the alteration of stibnite in sulphide deposits. Colloform sphalerite is a widespread mineral in low-temperature deposits, particularly those of the Mississippi-Valley type. We identified valentinite and colloform sphalerite in hydrothermal deposits occurring in the Baia Mare area. The Baia Mare metallogenic district of Neogene age occurs in the northwestern part of the Neogene volcanic chain within the Eastern Carpathians. The Neogene volcanism from Baia Mare area is related to the subduction processes of the East European plate under two microplates, Alcapa and Tisza-Dacia/Tisia, in the post-collisional compressive phase. We have identified valentinite in the Dealul Crucii and Baia Sprie deposits, associated with other epithermal minerals, in the absence of the stibnite. Valentinite is deposited in the final phase of the epithermal process after calcite and manganese-bearing calcite. Micro-Raman and microprobe determinations indicate the presence of valentinite. The formula of valentinite is close to stoichiometric Me_2O_3 and contains small amounts of tin as an antimony substituent. Colloform sphalerite was identified in the Baia Sprie ore deposit associated with minerals formed in the final epithermal phase. It was deposited on idiomorphic crystals of stibnite, which it corrodes. Its structure and an alternate banding, exhibited on the nano-/microscale, were identified by optical microscopy, SEM (scanning electron microscopy), and BSE (backscattered electron microscopy) imaging. These structures are typical for colloform sphalerite and suggest a genesis due to episodic precipitation. The spherical nano/micro-particles (nodules) are characteristic of the colloform sphalerite from Baia Sprie. Raman analysis indicates the presence of a colloform sphalerite with low iron content. The typical diffraction lines for sphalerite were identified in X-ray diffraction: 3.118 Å (111), 1.907 Å (220), 1.627 Å (311). Microprobe analysis certifies the presence of sphalerite with the stoichiometric formula close to ZnS. Iron content is low (0%–0.0613%), but Sb (0.7726%–2.6813%), Pb (0.56%–1.1718%), Bi (0%–0.1227%) are also present. The negative correlation between Zn and Sb suggests the simultaneous deposition from the same epithermal fluids. Valentinite and colloform sphalerite were formed at low temperatures (100–150 °C) at the end of the epithermal process.

Keywords: valentinite; colloform sphalerite; Dealu Crucii; Baia Sprie; Baia Mare; Eastern Carpathians

1. Introduction

Valentinite and colloform sphalerite are very rare minerals in epithermal deposits. Valentinite has been discovered in the Dealul Crucii (Crucii Hill) and Baia Sprie ore deposits and colloform

sphalerite in Baia Sprie ore deposits, respectively (Figure 1) [1]. Hydrothermal ore deposits from Baia Mare mining district are internationally recognized for the minerals that were first described here: andorite [2], semseyite [3], felsöbanyite [4], klebelsbergite [5], dietrichite [6], szmikite [7], in the Baia Sprie area, fülöppite [8] Dealul Crucii, and fizélyite [9] at Herja.

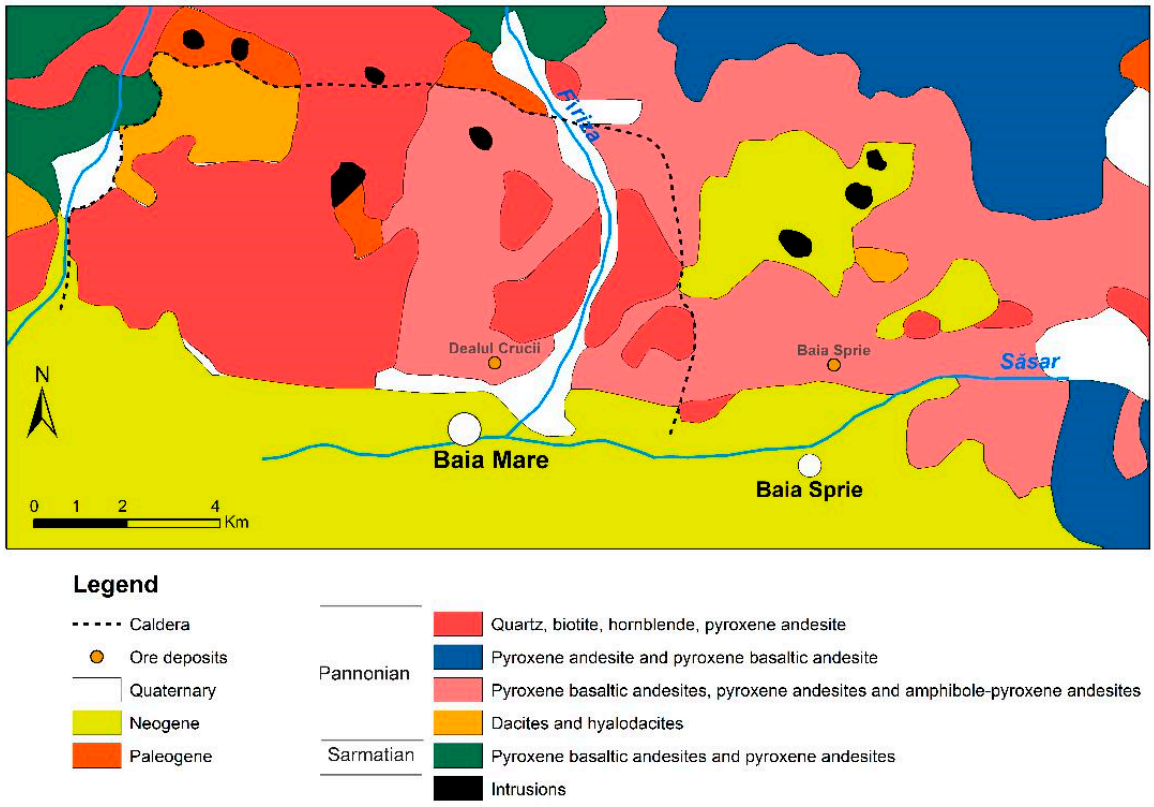

Figure 1. Sketch of the map of Baia Mare area with the location of ore deposits Dealul Crucii and Baia Sprie, with modifications after [1].

Valentinite occurs in many locations around the world, for example, in France at Chalanches mine, north of Allemont, Isere, and in other occurrences [10]. They are formed during the alteration process of stibnite and other minerals rich in antimony and are associated with senarmontite and kermesite.

Colloform sphalerite occurs in low-temperature deposits, especially those of the Mississippi-Valley Type (MVT) in carbonate-hosts [11]. According to this author, colloform sphalerite is cryptocrystalline to fibrous and shows a banded structure. The origin of colloform sphalerite has been discussed by Rogers (1917) [12], indicating that it was formed from colloidal and meta-colloidal substances, in the open space. There were authors who indicated the non-colloidal origin of the colloform textures [13,14]. Roedder (1968) [13] demonstrated by electron-microprobe analysis (EMP) and scanning electron microscopy (SEM) that the banded structures of the Pine Point field (Northwest Territories, Canada) are due to the variation in iron content. Pfaff et al. (2011) [15] supported that colloform now is mostly accepted as a descriptive morphological and not as a genetic term.

MVT ore deposits occur in Pine Point Canada [13], in Wisconsin, Missouri, Illinois states from USA [16–18], in Réocin, Noth Spain, in Trèves, South France, and Krakow-Silesia, Poland [19].

A major MVT deposit is located in the Wiesloch area of southwest Germany, which is controlled by the graben-related faults of the Upper Rhinegraben [19]. This deposit occurs in Middle Triassic limestones [19]. The Schwarzwald ore district is located in the southern part of the Wiesloch MTV deposits. The hydrothermal veins in the Schwarzwald ore district are comparable to the formations from the Wiesloch MVT deposit [15].

Colloform sphalerite also occurs in the Bleiberg Pb-Zn deposit in the Drau Range (Eastern Alps) in Alpine-Type (APT) Triassic carbonate-hosted. In this deposit, different types of sphalerite: colloform schalenblende and crystalline sphalerite, co-occur in the same sample [20].

In the present study, we examine the occurrence of valentinite and colloform sphalerite from epithermal ore deposits from the Baia Mare area, Eastern Carpathians. The aim of this study is to characterize these minerals, formed at low temperatures.

2. Geological Settings

The metallogenetic district of Baia Mare represents the northwestern part of the Neogene Volcanic Chain from the inner side of the Eastern Carpathians. This volcanic chain was formed during the Neogene geotectonic evolution of the Carpathian-Pannonic region, by the Miocene subduction of the Eastern European plate under two continental/microplate blocks, Alcapa and Tisza-Dacia/Tisia [21–23], (Figure 2a). The Neogene volcanism from Baia Mare area is related to the subduction processes from the Orogenic Carpathian chain in the post-collisional compressive phase. Magmatic activity in Baia Mare is connected to the intensification of the extension system of the Transcarpathian Basin [24].

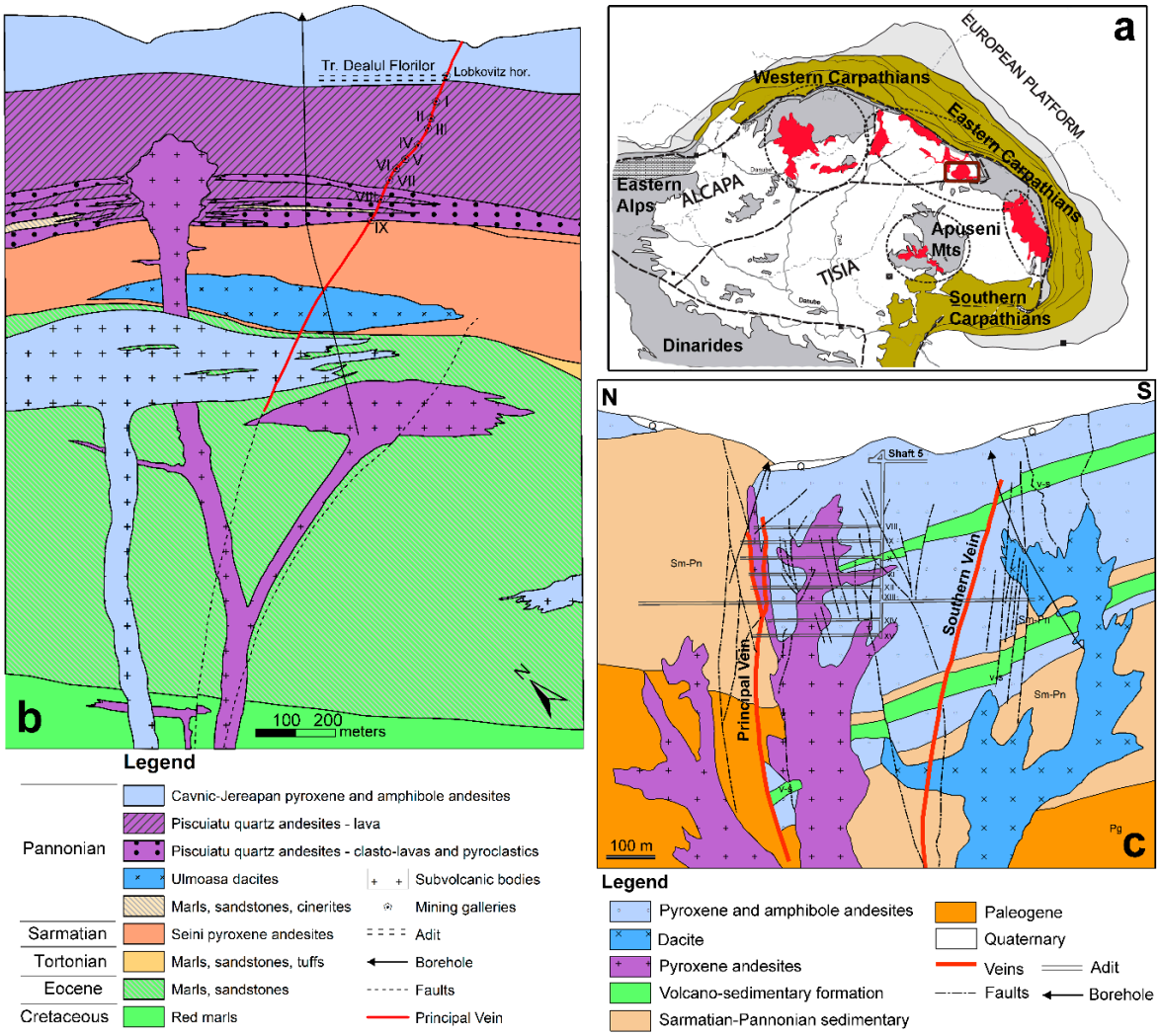

Figure 2. (**a**) Samplified Carpathian–Pannonian region map with the location of BaiaMare district [23]; (**b**) geological cross-section of Dealul Crucii [25]; (**c**) geological cross-section of Baia Sprie deposit eastern part [26].

The magmatic activity began with the explosive calc-alkaline (rhyolite-rhyodacite) acid phase Lower-Badenian-Lower-Sarmatian (Bugloviane) age [27]. According to Szakács et al. (2012) [28], this volcanic activity starts in Badenian (~14.8–15.1 Ma). In the Gutâi Mountains, the intermediate volcanism occurred in the second (Sarmatian-Pontian) and third cycle (Upper Pliocene) [27–29]. Using K-Ar dating [30], it was proved that the calc-alkaline intermediate volcanic activity was restricted between Sarmatian-Pliocene to Lower Sarmatian-Pannonian when we refer to different types of andesites and dacites as lava flows (13.4–9.0 Ma) and small basaltic intrusions (8.0–6.9 Ma). The Neogene volcanic and sub-volcanic structures in the Baia Mare area intruded the basement of the Lower Cambrian metamorphic rocks, the Paleogene Trans-Carpathian flysch sequence, and Neogene molasse sediments.

The intrusive magmatic activity occurred later than or coincidently with the lava flows of the calc-alkaline intermediate volcanism. The bodies of intrusive magmatic rocks from the Oaş-Gutâi have different morphological characters: stocks, dykes, apophyses, sills, microlaccolithes. Microdiorites, quartz-diorites, quartz-monzodiorites, microgranodiorites, and tonalites represent the intrusive rocks [31]. These intrusive bodies have an important role in the localization of ore deposits.

According to data presented by Giuşcă et al. (1973) [24], as well as radiometric data [30] in the Gutâi Mts., one could note the development of volcanism from west to east and from south to north. The evolution of magmatism from West to East within the Gutâi Mts. was explained by Popescu (1994) [32] through a compressive stress condition in the first stage before Badennian and extensive stress conditions in Sarmatian-Pannonian.

The metallogenetic activity would correspond to three distinct phases [24]: Sarmatian, Pannonian, Pontian. It overlaps with the calc-alkaline intermediate magmatic activity from the second eruption cycle. According to the K-Ar and Ar-Ar dating [33], the metallogenetic activity is restricted to the Pannonian level (11.5–7.9 Ma.). Analyzing this data, two phases can be deduced in the Gutâi Mountains, one in the western zone (Ilba-Nistru–Săsar-Herja) and the second in the eastern zone (Baia Sprie-Şuior-Cavnic-Băiuţ).

Damian et al. (2003) [34] suggested that the metallogenetic activity in the western zone is associated with the formation of two calderas in the Sarmatian and Pannonian. In the eastern part, it is associated with the W–E trending Bogdan Vodă–Dragoș Vodă fault system, located in the southern part of Gutâi Mountains [32–35]. This transcrustal fault localized the development of the volcanism and of the metallogenesis [36]. It is also possible that it had the role of a releaser and also a localizer in the surrounding spaces, along with the support fractures of the ore deposits [37].

In our opinion, for the entire Baia Mare area, metallogenesis would correspond to a single-phase, during Pannonian. Within this metallogenetic phase, three mineralization stages can be separated: a copper one, a base-metallic one, and a gold-silver one, which are very clearly separated in time. In the western part, the mineralization has horizontal zonality [38]), while in the eastern part, it has a vertical one. This vertical zonality is very clearly exhibited at Baia Sprie: silver-gold, base-metal, and copper [39].

The structural control, the association with magmatic intrusions, the mineralogical composition of the ores, and the association with different types of hydrothermal alteration are related with mineralizations of a low sulfidation epithermal system.

In the Baia Mare area, the ore deposits are predominantly base-metallic, but gold-silver and copper mineralizations also appear. The upper parts of the copper and base-metallic mineralizations have important quantities of gold and silver. The ore deposits appear predominantly as veins, but breccia bodies and stockworks are also known. The upper parts of these veins are very branched-out and have stockwork type mineralization where gold-character is predominant. Within the base-metallic veins, a zonal distribution of mineral character can be observed, while the gold veins and the smaller dimensional ones are lacking this character. The hydrothermal alterations associated with the mineralizations are represented by phyllic ones, while in the upper gold parts, the potassic (adularia type) and argillic ones are characteristic. Chloritization and phyllic alterations are associated with the copper mineralization.

2.1. Dealul Crucii Ore Deposit

The Dealul Crucii ore deposit is located north of the city of Baia Mare and represented a highly productive structure from the Middle Ages until recently (Figure 1). The structure of the Dealul Crucii (Figure 2b) is made up of volcanic rocks disposed over red marls (Upper Cretacic), marls and sandstones (Eocen), marls and pyroclastic rocks (Badenian), marls and sandstones (Pannonian) [25]. The volcanic rocks are represented by the Seini pyroxenic andesite lava flows (Sarmatian), quartz andesite from Piscuiatu (Pannonian), and pyroxene andesites from Piscuiatu. These last ones are dated Pontian after Nedelcu et al. (1970) [25], while using radiometric data, they are considered to be Pannonian [29]. The succession of sedimentary and volcanic rocks is intruded by sub-volcanic bodies represented by dacites, quartz andesites, andesites with pyroxenes and amphiboles [25].

The mineralization consists of a main vein and the branch bed: Cioara I, Cioara II. In the north of the Main vein, the smaller branches are: Sigismund, Rătăcit, and Baptist [25]). The Main vein of the Dealul Crucii has an extension of over 1000 m with a thickness of 1–8 m, exceptionally 15 m [25], and depth developed up to 700 m [40]. The mineralization of the Dealul Crucii was mined from the altitude of 511 m to the lower horizon of −75 m.

Ghiţulescu (1932) [40] separated the Dealul Crucii vein in three main areas:

- An upper part of golden quartz close to the surface;
- A silver-rich area with many silver minerals, dominated by pyrargyrite, which develops up to the Vth horizon (+40 m).
- The area of gold associated with sulphides between +40 m to −71 m. Here, the silver minerals are rare. Sulphides, especially pyrite, and small quantities of sphalerite, galena, and chalcopyrite with small gold inclusions are predominant.

The Dealul Crucii vein was intercepted at about 200 m below the last horizon (horizon IX). According to Nedelcu et al. (1970 [25]), the vein consists of two branches at this level. The first branch, with a thickness of 1.25 m, has massive mineralization consisting of galena, sphalerite, pyrite, chalcopyrite, marcasite associated with grey quartz and calcite. The second branch, with a thickness of 3.4 m, contains compact grey quartz with pyrite and plumosite, and possibly other sulfosalts. Near the vein, the predominant alteration is adularization, while phylic alteration is developed externally [30].

Dealul Crucii [41] is the type of locality of fülöppite, while another 25 minerals have been described here. Mineralization is very rich in sulfosalts: andorite, fülöppite, jamesonite, pearceite, semseyite, zinkenite. Nedelcu et al. (1970 [25]) consider the mineralization of the mesotermal-epithermal type, but according to its characteristics, it is a typical low-sulphidation epithermal mineralization. The ore deposit is located in the southeastern part of the Săsar Caldera [34].

2.2. Baia Sprie Ore Deposit

An update of the geological and metalogenetic data for the Baia Sprie ore deposit was recently made by Buzatu et al. (2015) [26]. This deposit is the most important one in the Baia Mare area, and it has been mined continuously from the beginning of the 14th century [39] until 2006. This deposit is located along the Bogdan Vodă–Dragoș Vodă fault system, in the southern part of Gutâi Mountains [32,35,42].

The geological structure of the area consists of sedimentary formations of Badenian, Sarmatian, Pannonian, and magmatic Pannonian rocks, [36,39,43]. The volcanic deposits are represented by volcano-sedimentary formations: pyroclastic products, explosion breccias, and lavas [39]. The main lava flows are represented by: amphibole–pyroxene andesites, pyroxene-amphibole-quartz andesites, quartz-bearing andesites, pyroxene-basaltic andesites. The amphibole–pyroxene andesites have the greatest spatial distribution and are the main rocks composing Dealul Minei. They are identic with the Jereapan andesites. They are Pontian, while, according to radiometric data, Pannonian [29]. The amphibole–pyroxene andesitic body is considered to be a dyke (E–W) with a north-oriented slope. These structures were interpreted by Iștvan et al. (1996) [1] as a graben, delimited by the Main vein

and by the new vein. The Jereapan type andesite (amphibole–pyroxene andesite) lava flow is intruded by bodies of massive pyroxene-andesites and dacite [44]. According to the geological cross-section of Baia Sprie deposit through the fifth shaft—eastern part, we interpreted the geological structure to be a "trapdoor" caldera similar with the one that was described at Roşia Montană [45]. This caldera is delimited in its northern part by the W–E trending Bogdan Vodă–Dragoș Vodă fault system, located in the southern part of Gutâi Mountains [32,35,42].

Metalogenetic activity was determined by the tectonic and magmatic events along the W–E trending Bogdan Voda-Dragoș Vodă fault system [32,35,42], which triggered the magma activity and the intrusion of the subvolcanic bodies associated with the mineralization from Baia Sprie. The Main vein developed along the faults located at magmatic-sedimentary contacts or near the intrusions. There are several branches inside the andesite body and within the lava flows located near the surface of the Minei Hill.

The Main vein from Baia Sprie is located on the Nordic dyke's contact. The vein has a length of 5250 m [46]. It is developed to more than 800 m in depth, with a thickness up to 22 m. The upper part in the Minei Hill included the vein branches with high gold and silver grades. The middle part of the vein's mineralization has mainly a lead-zinc character, and it has a copper character below horizon X. The Nou vein is placed in the southern part at the contact between the andesitic dyke and the sedimentary formation. It has a length of 2100 m, a maximum thickness of 6 m, with a vertical development of 200 m [29,39,43]. The mineralization has a lead-zinc character. Between the Main vein and Nou vein, at the XI and the XIV horizons, there are two other veins: the Diagonal and the Terezia. The Diagonal vein has a lead–zinc character similar to Nou vein. The Terezia has a pyrite–copper mineralization.

Host rocks around the veins were severely affected by hydrothermal alteration (Stanciu, 1973 [47]). The wall rock alteration precedes the metallogenetic activity and exhibits a distinct vertical and horizontal zonality in the vicinity of the veins [46]. At higher depths, a chlorite alteration is associated with copper mineralization. The zinc-lead mineralization is associated with a phyllic alteration. Argillized and adularized alterations are associated in the upper area of the branches of the Minei Hill vein.

The spatial distribution of the mineralization in the Main vein suggests its zonal character. Mineralization was formed in two distinct phases: in the first phase copper mineralization, while in the second phase, the lead-zinc and gold-silver mineralization. Gold-silver mineralization is predominant in the upper part. At horizon XII, copper mineralization is crossed by lead-zinc mineralization.

The Baia Sprie ore deposit is the most complex one in terms of mineralogical composition. This ore deposit has an impressive wealth of mineralogical associations, with over 94 minerals described so far. The deposit is the type locality for six minerals (andorite, semseyite, felsöbányaite, dietrichite, klebelsbergite, and szmikite) [39,48]. Manilici et al. (1965) [39], presented in detail the mineralogical composition for the Main vein from Baia Sprie, and Petrulian et al. (1971) [49] for the Nou vein. Superceanu (1957) [50] demonstrated the presence of wolframite in its investigation. A synthesis on the mineralogical composition of Baia Sprie was made by Damian et al., (1995) [46]. The mineralogical composition of Minei Hill's Main vein's branches was studied by Iștvan et al. (1996) [1] and Damian et al. (2003) [48], who described Ag sulfosalts, such as freibergite, stephanite, and pearceite–polybasite, associated with pyrargyrite and miargyrite.

Applying electron microprobe analysis or Raman spectrometry [51,52], determined in detail the weathering mineral products and the Fe content in sphalerite. A new occurrence of bismuth minerals has been identified using electron microprobe analyses on the Baia Sprie samples by Buzatu et al. (2015) [26]: bismuthinite, lillianite–gustavite series, disordered intergrowths of lillianite homologues, heyrovskýite, and cosalite.

3. Methods and Materials

The chemical compositions were determined using a Cameca SX-100 Electron Probe Microanalyzer (EPMA). The analyses were carried out at the State Geological Institute of Dionyz Stur (Bratislava, Slovakia). The analysis points were selected using the backscattered electron (BSE) images. The measurements were performed on polished carbon-coated sections using an acceleration voltage of 25 kV and a 15–20 nA beam current, 5 μm beam diameter, 20 s integration time for the peak, and 7 s for the background. The following X-ray lines from the natural (n) and synthetic (s) standards were used: S Kα (n-$CuFeS_2$), Fe Kα (n-$CuFeS_2$), Pb Mα (n-PbS), Cu Kα (n-$CuFeS_2$), As Kα, Lα (n-FeAsS), Sb Lβ (n-Sb_2S_3), Se Lβ (s-Bi_2Se_3), Zn Kα (n-ZnS), and pure metals for Ag Lα, Bi Lα, Cd Lα, and Mn Kα.

The sphalerite samples were analyzed by X-ray diffraction (XRD, Faculty of Physics, Alexandru Ioan Cuza University of Iaşi, Romania), using a Shimadzu LabX XRD-6000 diffractometer. The measurement conditions were: Cu anode, 40 kV accelerating voltage and 30 mA cathode current, divergence slit 1.00°, scatter slit 1.00°, receiving slit 0.30 mm, scan range 5–90.0, continuous scan, scan speed 0.6°/min, sampling pitch 0.02°, preset time 2 s.

The crystal habit of the identified minerals was studied by scanning electron microscopy (SEM, Faculty of Biology, Alexandru Ioan Cuza University of Iaşi, Romania) (gold coated samples), using a Tescan Vega II SBH instrument.

The ZEISS AXIO IMAGER A2m chalcography microscope was used with the EC EPIPLAN-NEOFLUAR 10X/0.3 and 20X/0.5 objectives and with the PL 10x/23 eyepieces for a primary identification and characterization of the observed minerals. The backscatter electron detector from a Hitachi Tabletop TM3030 (Geological Institute of Romania, Bucharest, Romania) was used for BSE imaging, with a tungsten filament, in high vacuum with an EHT of 20 kV and a working distance of 8.5 mm.

The non-polarized micro-Raman spectra of valentinite samples were recorded in the spectral range 50–1200 cm^{-1}, using a Horiba Jobin-Yvon–LabRam HR 800 micro-Raman Spectrograph (Geological Institute, Slovak Academy of Sciences, Banská Bystrica, Slovakia). The 632.8 nm excitation line of a He-Ne laser (17 mW) was focused with a 100×/0.80 Olympus objective on the sampled surface. The experimental parameters were: 30–50 s integration time, 6 acquisitions diffracted on a 600 lines/mm grating. Neutral density filters were used to control the laser power in order to avoid sample heating and damaging. The grating turret accuracy was calibrated between zeroth-order line (180° reflection) and laser line at 0 cm^{-1}. Spectral accuracy was verified using silicon's ν_1 peak, which was always lying within three detector pixels around the theoretical value (520.7 cm^{-1}). The system resolution was 2 cm^{-1}, and the wavenumber accuracy was ±1 cm^{-1}.

The Raman spectra of the colloform sphalerite samples were acquired using a Horiba Jobin–Yvon RPA–HE 532 Raman Spectrograph (Department of Geology, Alexandru Ioan Cuza University of Iaşi, Romania) with a multichannel air-cooled (–70 °C) CCD detector, using a frequency doubled Nd:YAG laser at 532 nm at a nominal power of 100 mW. The spectral range was 200–3400 cm^{-1}, and the spectral resolution was 3 cm^{-1}. The Raman system includes a "Superhead" fiber-optic Raman probe for non-contact measurements, with a 50X LWD Olympus objective used in the visible optical domain. Sulphur and cyclohexane bands were used for Raman spectra frequency calibrations. The spectra were acquired using 2 s exposures, 30 acquisitions, at a laser power of 70%, in order to improve the signal-to-noise ratio.

The valentinite and colloform sphalerite samples described in this study are from the collection of the County Museum of Mineralogy "Victor Gorduza" Baia Mare.

4. Results and Discussions

4.1. Valentinite

Valentinite was first mentioned at Baia Sprie by Koch (1923) [53] and Tokody (1942) [54]. We identified valentinite in samples from Baia Sprie and Dealul Crucii. In these occurrences, it appears in the epithermal veins associated with minerals deposited in the final phases of the metallogenetic process. It appears as prismatic crystals (Figure 3a), elongated, lamellar, or granular, associated with carbonates, sphalerite, chalcopyrite, and tetrahedrite developed in vugs. This form of presentation is like the one described by Koch (1923) [53] and Schaller (1937) [55]. At Baia Sprie, it appears in the form of lamellar crystals associated with quartz and manganese-bearing calcite. At the Dealul Crucii, crystals smaller than 1 mm are placed on calcite crusts or are associated with idiomorphic calcite crystals. Quite often, the valentinite lamellae are placed on intergrowths between sphalerite, chalcopyrite, and tetrahedrite with large amounts of silver (Figure 3b).

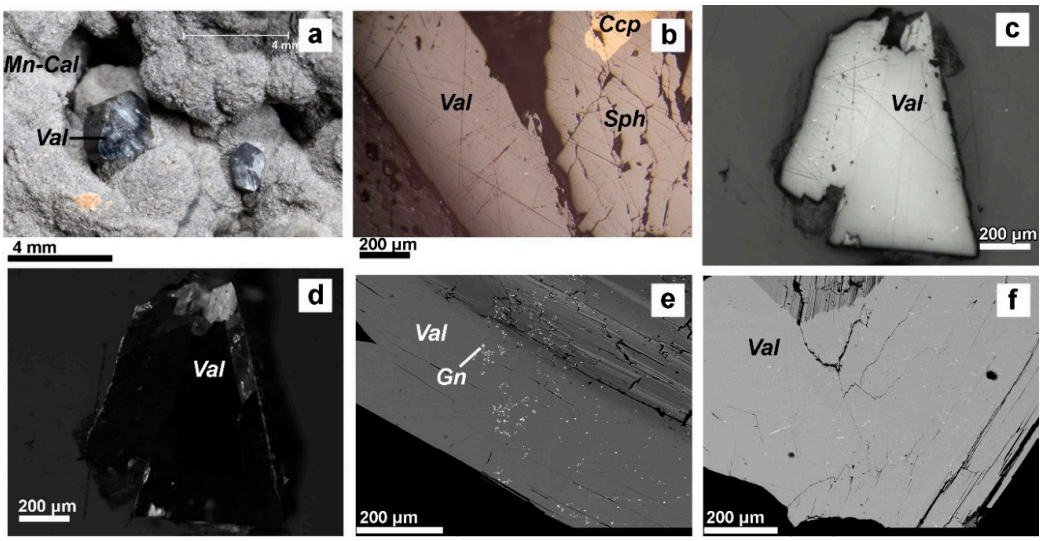

Figure 3. Macroscopic, reflected light, and backscattered (BSE) images: (**a**) macroscopic images of valentinite, (**b**–**d**) reflected light parallel and crossed polarizers; (**e**,**f**) BSE images. Val—valentinite; Sph—sphalerite; Ccp—chalcopyrite; Mn-Cal—manganese-bearing calcite.

Macroscopically they appear as grey, partially transparent, prismatic crystals with adamantine luster (Figure 3c,d). Bireflexion is evident in reflected light (Figure 3c), and anisotropy is blurred by semitransparency (Figure 3d). The evident anisotropy certifies the presence of valentinite because stibiconite and senarmontite crystallize in the cubic system so that they are isotropic. Backscattered electron images show nano-scale inclusions of galena in valentinite (Figure 3e,f).

The analyses carried out using the Cameca SX-100 Electron Probe Microanalyzer (EPMA) confirmed the presence of valentinite. In the previous studies of Koch (1923) [53] and Tokody (1942) [54], only crystallographic data was used to identify the valentinite from Baia Sprie and Dealul Crucii. The composition of Baia Sprie and Dealul Crucii valentinite is presented in Table 1. The antimony content ranges from 76.45%–79.64%. These quantities are smaller than the theoretical value of 83.53% reported by Palache et al. (1944) [56]. The composition of valentinite has a very small variability between the analyzed points. Usually, valentinite contains small amounts of tin (0.21%–0.23%) and sometimes lead, silver, bismuth, and iron. These elements replace the positions of the antimony in the structure of valentinite. The chemical analyses are close to that of the stibiconite's composition, but this mineral is isotropic and differs significantly from valentinite. The chemical formulas (Table 1) are very close to the stoichiometric formula of valentinite Me_2O_3. The presence of sulfur may indicate a slight state of supergene alteration with sulfates, which explains the lower antimony content.

Table 1. Electron Probe Microanalyzer (EPMA) results for valentinite from Baia Sprie and Dealul Crucii deposits.

No	Sample Name	SO_3	Ag_2O	PbO	Bi_2O_3	CuO	Sb_2O_3	FeO	SnO	Formula
47/1	BS-2680_an1	0.0133	0	0	0.0342	0	96.7938	0.0462	0.255	$Sb_{1.993}Sn_{0.006}Fe_{0.003}O_3$
48/1	BS-2680_an2	0	0	0	0.0348	0	95.465	0	0.2559	$Sb_{1.996}Sn_{0.006}O_3$
49/1	BS-2680_an3	0	0	0	0	0	95.0205	0.0407	0.2758	$Sb_{1.995}Sn_{0.006}Fe_{0.002}O_3$
53/1	DC-2108_an3	0	0.028	0	0	0	93.892	0	0.2592	$Sb_{1.996}Sn_{0.006}O_3$
54/1	DC-2108_an4	0.0032	0	0.0309	0	0.009	96.8374	0	0.2669	$Sb_{1.995}Sn_{0.006}O_3$
55/1	DC-2108_an5	0.0063	0	0	0	0	95.4937	0	0.2599	$Sb_{1.996}Sn_{0.006}O_3$
56/1	DC-2108_an6	0	0.011	0	0.0007	0	93.227	0.025	0.2654	$Sb_{1.995}Sn_{0.006}Fe_{0.001}O_3$

The micro-Raman spectra of valentinite samples (Figure 4a,b) show a very good signal with clear and sharp peaks. The spectra are dominated by very intense bands at 141, 216, 295, and 501 cm^{-1}. Besides these bands, typical valentinite lines appear below the 400 cm^{-1} region at 76, 106, 187, 225sh (sh—shoulder) and 284sh cm^{-1}. In the higher region of the spectra, bands are observed at 444, 489sh, 596, and 683 cm^{-1}. All these peaks are in a very good agreement with those previously reported in the literature [57–59]. As regarding the band assignments, the Raman lines below 400 cm^{-1} can be attributed to the external lattice modes, controlled by the unit cell and crystal space group of the structure [59]. The 400–700 cm^{-1} region is characterized by internal modes of symmetric/ antisymmetric stretching and bending of Sb–O–Sb bonds from the SbO_3 pyramids. These modes are classified as follows: antisymmetric bending—444 cm^{-1}, symmetric bending—489sh and 501 cm^{-1}, antisymmetric stretching—596 cm^{-1}, and symmetric stretching—683 cm^{-1} [59]. The micro-Raman results for the DC-2108 sample (Dealul Crucii) showed one additional band at 258 cm^{-1}, which might be attributed to the presence of the cubic form of Sb_2O_3, senarmontite [57–59].

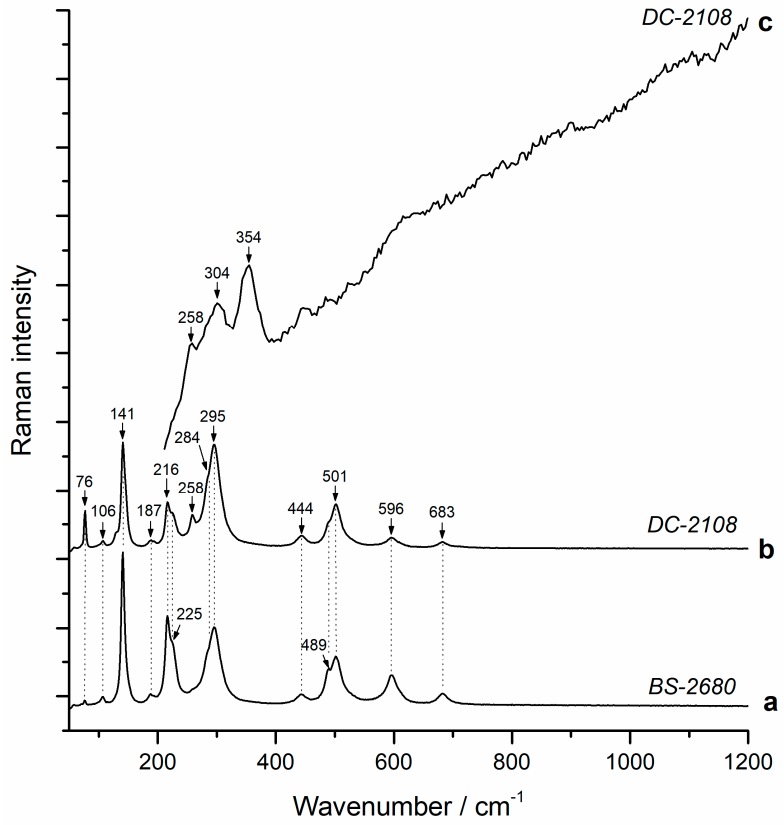

Figure 4. Raman spectra of valentinite samples from Baia Sprie (**a**) and Dealul Crucii (**b**); Raman spectrum of colloform sphalerite (**c**).

4.2. Colloform Sphalerite

Colloform sphalerite is typical for MVT mineralizations of Wisconsin, Missouri, Illinois [17], Southwest Germany, France and Krakow-Silesia, Poland [19]), in the Drau Range (Eastern Alps) in Alpine-Type (APT) Triassic carbonate-hosted [20] and is not specific to epithermal mineralization. One of the main results of this study is the identification of colloform sphalerite in the epithermal intermediate type Baia Sprie ore deposit, proving the possibility of its formation in such a system.

Colloform sphalerite has a yellowish colour and overgrows on idiomorphic crystals of stibnite because it is formed later than them (Figure 5a,b). Compared to MVT colloform sphalerite, the colour of the described samples is homogeneous. The colour banding of MVT is due to variations in FeS content [17]. Analyzing our polished sections in reflected light, this mineral is clearly distinguished from the stibnite by its dark grey colour and isotropy (Figure 5c–e). It partially replaces the stibnite crystals on which it is deposited (Figure 5d). It forms band-shaped deposits around the stibnite crystals (Figure 5d,e), resulting in tubes of several mm or cm. Inhomogeneous masses of earthy aggregates of colloform sphalerite are deposited between the stibnite and quartz crystals (Figure 5c,f), indicating its formation after stibnite in ore mineral sequence. Quartz inclusions and holes frequently appear in these masses.

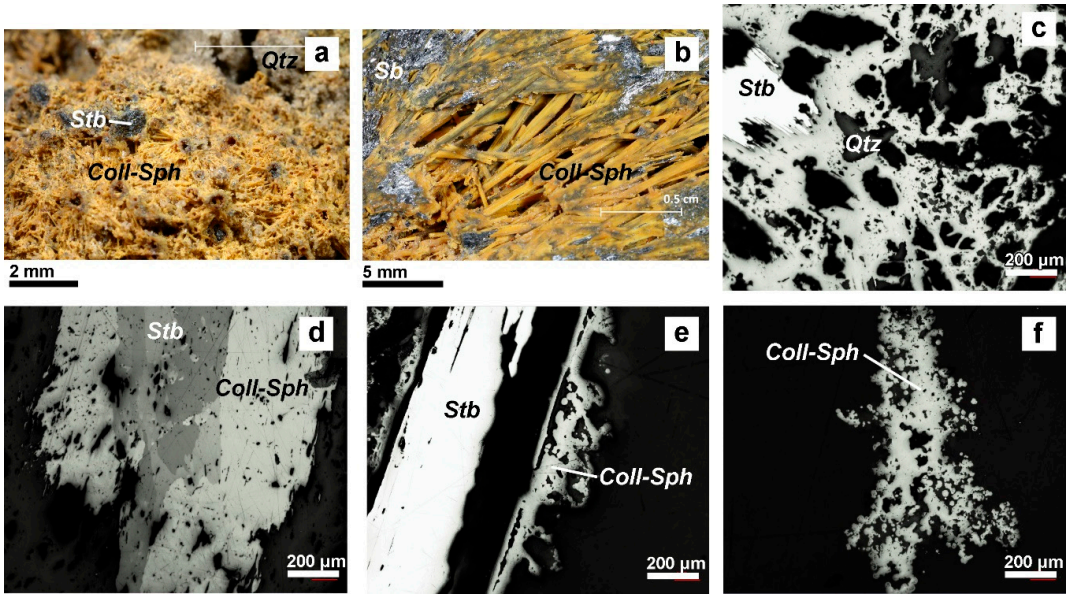

Figure 5. Macroscopic and reflected light images: (**a**,**b**) colloform sphalerite (Coll-Sph), quartz (Qtz), and stibnite (Stb); (**c**,**e**) stibnite (Stb) and colloform sphalerite (Coll-Sph) parallel polarizers; (**d**) stibnite (Stb) and colloform sphalerite (Coll-Sph) crossed polarizers; (**f**) earthy aggregates of colloform sphalerite (Coll-Sph) parallel polarizers.

The colloform sphalerite deposits on stibnite can be very well-identified in the SEM images (Figure 6). These nano/micro-wires can have thicknesses of several microns (Figure 6a–f) forming tubes of several mm or cm in length around the stibnite crystals. These tubes resulted from leaching of antimony from stibnite. Compact masses of colloform sphalerite rarely appear (Figure 6f,g). Spherical nano/microscale particle deposits smaller than 20 µm are present at the surface and inside the tubes. These are obvious in Figure 6h where the dimensions are below 10 µm and the constituents of the agglomeration are micron and submicron-sized nanowires. These nodules are like those obtained for synthetic sphalerite by Ibupoto et al. (2013) [60] through the hydrothermal method.

These nodules appear in the colloform porous sphalerite, where many holes can be seen, as shown in the images in Figure 5c,f and can be very well observed in the BSE images (Figure 7). They are deposited especially on the outside of the colloform sphalerite deposits, on the stibnite (Figure 7a,b),

or in the holes inside the porous masses (Figure 7c). Their morphology is composed of nodular nano/microscale clusters (Figure 7d,e). The dimensions of a nodule do not exceed 20 µm. The polished nodules (Figure 7f) have the same composition as the bulk colloform sphalerite in which they are included. Microscale inclusions of goslarite, resulting from the supergene alteration of the colloform sphalerite, are frequent in the earthy aggregates (Figure 7b.)

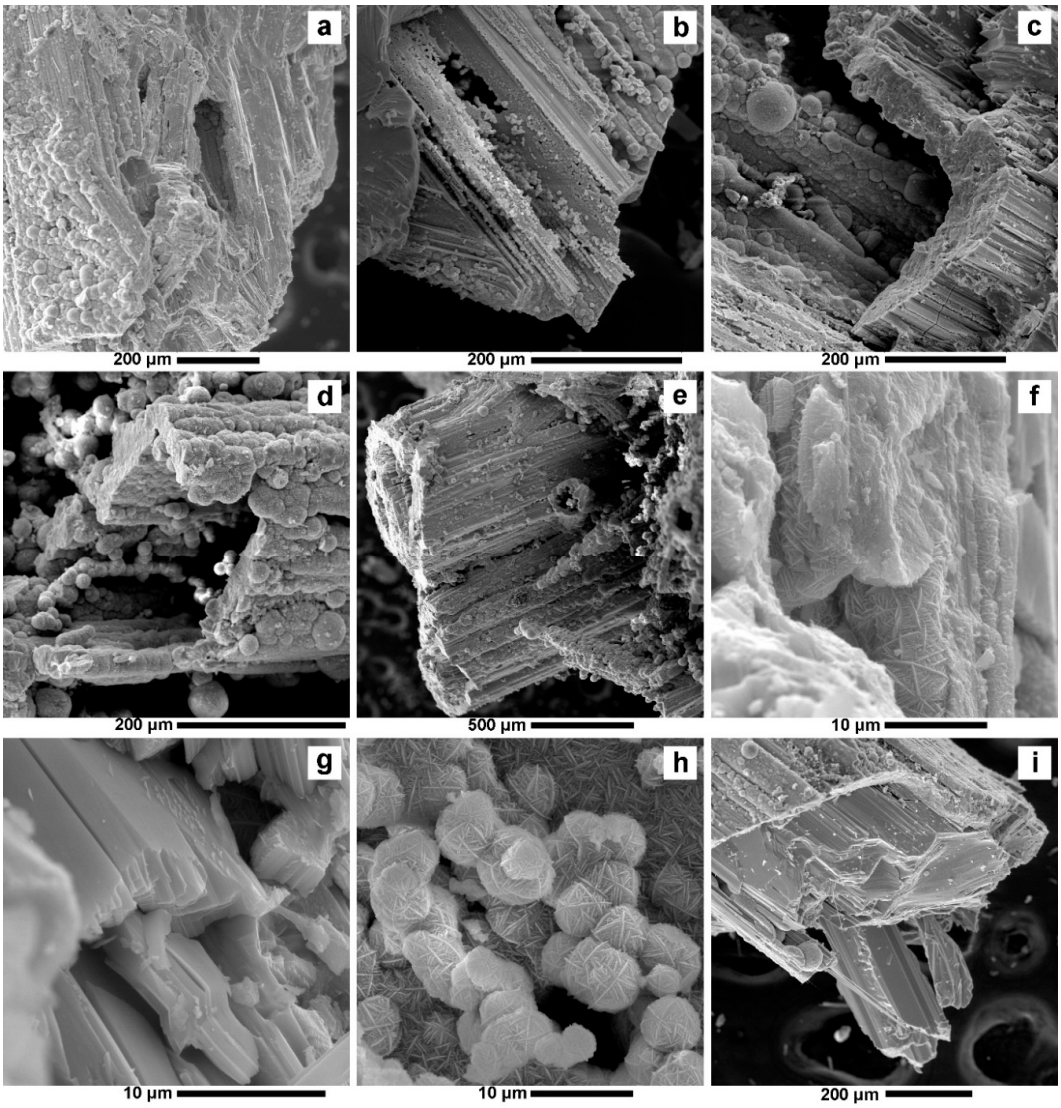

Figure 6. Scanning electron microscopy (SEM) images of: (**a**–**e**) colloform sphalerite tubes deposited on stibnite crystals; (**f**,**g**) compact masses of colloform sphalerite; (**h**) submicron-sized nanowires of colloform sphalerite forming spherical particles; (**i**) colloform sphalerite of stibnite.

The colloform structures can be very well observed in the BSE images from Figure 8 obtained using the Cameca SX-100 EPMA. They consist of micro-scale alternating bands up to 1000 µm, showing a laminated fabric. The nodules described above appear interspersed between these bands, which is the characteristic colloform sphalerite texture. Outwardly, the bands become irregular on a micro-scale. They contain many nodules between the alternating bands. This fabric suggests a genesis due to episodic precipitation of sphalerite. This can be achieved by repeated short-term mineralization pulses [20]. The earthy aggregates (Figure 8b) have a porous appearance due to a high number of holes.

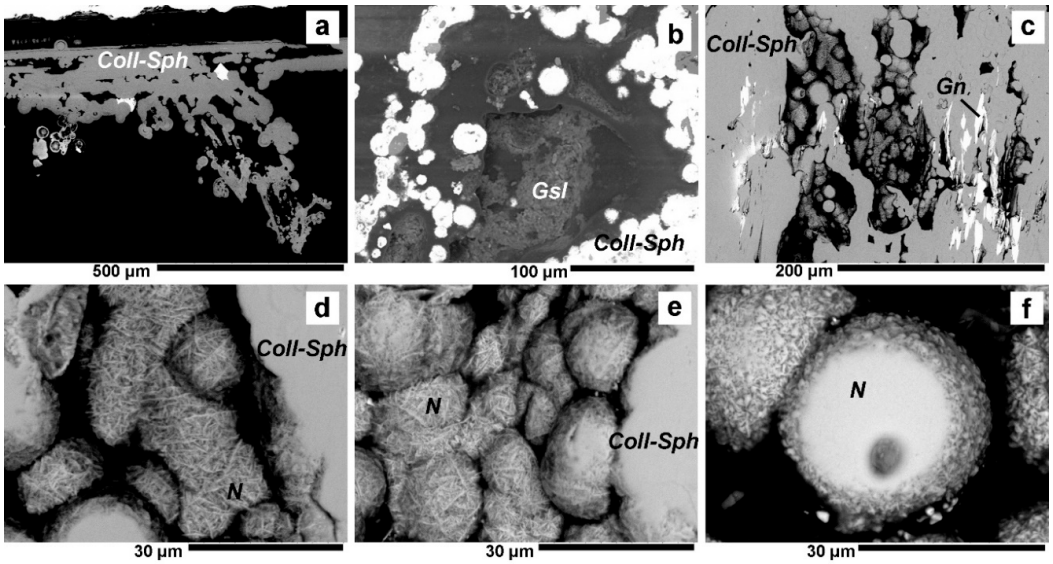

Figure 7. BSE images obtained using the backscatter electron detector equipped with the Hitachi Tabletop TM3030: (**a,b**) nodules of colloform sphalerite (Coll-Sph) associated with goslarite (Gsl); (**c**) porous masses with galena (Gn) inclusions; (**d,e**) nodular nano/microscale clusters of colloform sphalerite; (**f**) polished nodules of colloform sphalerite (N).

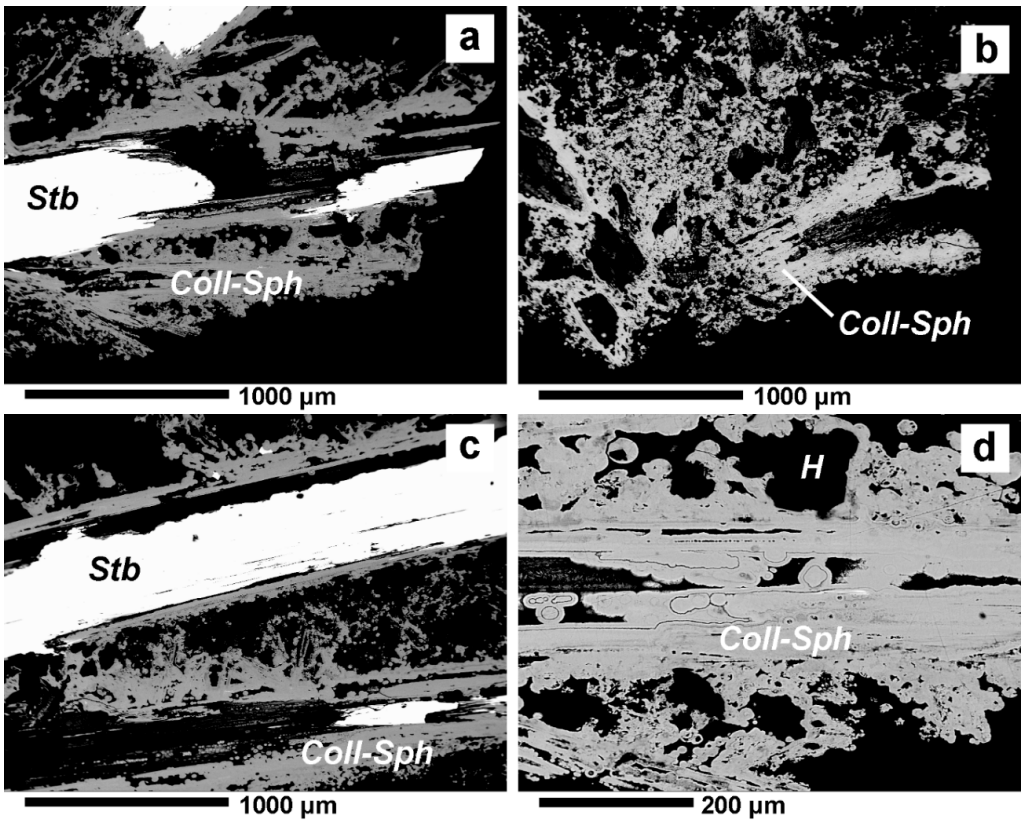

Figure 8. BSE images showing specific fabric of colloform sphalerite: (**a,c**) alternating bands of colloform sphalerite (Coll-Sph) associated with stibnite (Stb); (**b**) earthy aggregates with high porosity; (**d**) nodules and holes (H) between laminated colloform sphalerite.

The XRD diffraction study of colloform material indicates the presence of sphalerite (Figure 9). XRD analyses were performed using a Shimadzu LabX XRD-6000 X-ray diffractometer. The main diffraction lines that certify the presence of the sphalerite are: 3.118 Å (111), 2.70 Å (200), 1.907 Å (220),

1.627 Å (311), 1.35 Å (400), 1.238 Å (331), 1.101 Å (511, 333). The diffractogram is the same as that from ASTM no. 5-566 [61]. The presence of large quantities of high crystallinity spherite is indicated by the thin, tall, and sharp diffraction lines. The weak peak at 3.30 Å can be associated with the reflection from the $10\bar{1}0$ (100) crystallographic plane of würtzite. Its low intensity indicates that this mineral is present in very small quantities. The other diffraction peaks are not obvious because they are partially covered by the very intense 3.118 Å peak from sphalerite. This peak also covers the würtzite peaks from 3.128 Å (002) and from 2.925 Å (101).

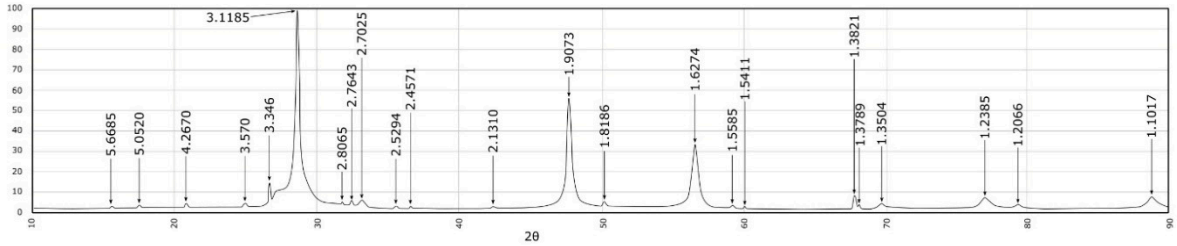

Figure 9. X-ray diffraction (XRD) of colloform sphalerite (Coll-Sph).

Small amounts of stibnite and quartz were also identified along with the ones from sphalerite (Figure 9). Stibnite is certified by the diffraction lines at 5.668 Å (020), 5.052 Å (120), 3.37 Å (130), 2.764 Å (041), 2.702 Å (301), 2.529 Å (240). Quartz is certified by the presence of the diffraction lines of 4.26 Å, 3.346 Å, 2.457 Å, 1.818 Å. Large amounts of sphalerite in the shape of crusts are deposited on aggregates of quartz and stibnite. The remaining line that is weakly observable at 2.806 Å indicates the presence of gypsum impurities, which were also observed under the stereomicroscope.

The Raman spectrum of colloform sphalerite is not so well-defined, being characterized by background noise and fluorescence (Figure 4c). This suggests that the sample is not a highly crystallized one, more likely to be of semi-amorphous composition. Nevertheless, from the Raman spectrum, three clear peaks can be distinguished at 258 cm^{-1}, 304 cm^{-1}, and 354 cm^{-1}. The first one was not reported so far for sphalerite, but it can be assigned to lattice modes in the unoriented sample. The 304 cm^{-1} and 354 cm^{-1} bands are typical for sphalerite, being similar to the ones from previous studies [52,62,63] with a slight shift of 4 cm^{-1} in the bands position. The Raman band assignments for sphalerite suggest that the ~350 cm^{-1} peak is due to Zn-S vibrations, while the ~300 and ~331 cm^{-1} are controlled by the vibration of Fe-S bonds [52,63]. In the present study, the line at ~331 cm^{-1} is missing or it is overlapped by the more intense band at 354 cm^{-1}, suggesting a sample with low Fe content [52].

The chemical composition (Table 2) of the colloform sphalerite granules analyzed under the microprobe indicates a variety poor in iron. The iron contents are much lower than those reported for the brown sphalerite from Baia Sprie (1.1–7.3 wt.% range) by Buzatu et al. (2013, 2015) [26,52] and for dark brown sphalerite from Cisma (Baia Mare) by Plotinskaya et al. (2012) [64]. This low iron content colloform sphalerite is also specific for the Wiesloch and Schwarzwald mineralizations in Germany [15]. Unlike the sphalerite of Cisma and Baia Sprie from the base metal mineralization, our samples do not contain Mn and Cd. They contain large amounts of antimony because they overgrow on idiomorphic crystals of stibnite. Large quantities of lead, between 0.56%–1.17% were also measured. The described samples contain small amounts of bismuth and sometimes copper. All these elements can substitute zinc's position in the sphalerite structure. The stoichiometric formulas are close to or identical to that of the ZnS (Table 2).

Table 2. Microprobe analysis results for colloform sphalerite.

Sample Codename	Cu	Fe	Bi	Sb	S	Pb	Zn	Total	Chemical Formula
2018_an1	0	0.0179	0.0329	1.5717	32.6581	0.7478	63.66	98.6879	$Zn_{0.97}Sb_{0.01}S_{1.01}$
2018_an2	0	0.0188	0	1.8936	31.9448	0.9229	63.1952	97.9753	$Zn_{0.97}Sb_{0.02}S_{1}$
2018_an3	0	0	0.0028	2.149	32.9386	1.1718	62.7512	99.0134	$Zn_{0.95}Sb_{0.02}Pb_{0.01}S_{1.02}$
2018_an4	0.0344	0.0613	0.0046	1.8271	31.7961	0.811	62.7965	97.331	$Zn_{0.97}Sb_{0.02}S_{1.01}$
2018_an5	0	0.0198	0	1.9453	31.8728	0.9271	62.6001	97.3651	$Zn_{0.97}Sb_{0.02}S_{1.01}$
2018_an6	0	0.0418	0.0176	1.8369	31.6313	0.7952	63.0341	97.3569	$Zn_{0.98}Sb_{0.02}S_{1}$
2018_an7	0.0127	0.0167	0	1.8427	31.9095	0.8546	62.601	97.2372	$Zn_{0.97}Sb_{0.02}S_{1.01}$
2018_an8	0	0.029	0.0183	1.5806	31.0534	1.0354	63.8626	97.5793	$Zn_{0.99}Sb_{0.01}Pb_{0.01}S_{0.99}$
2018_an9	0	0.0479	0.0344	0.7726	31.9911	0.56	65.0537	98.4597	$Zn_{0.99}Sb_{0.01}S_{1}$
2018_an10	0	0.0133	0.0226	1.4599	32.7883	1.0876	64.3684	99.7401	$Zn_{0.97}Sb_{0.01}Pb_{0.01}S_{1.01}$
2018_an12	0	0	0.0438	1.6283	31.5759	0.8551	63.5192	97.6223	$Zn_{0.98}Sb_{0.01}S_{1}$
2018_an13	0	0.0134	0	1.3705	32.2799	0.7191	63.9183	98.3012	$Zn_{0.98}Sb_{0.01}S_{1.01}$
2018_an14	0	0.0065	0	1.7952	31.8389	0.7561	63.5187	97.9154	$Zn_{0.98}Sb_{0.01}S_{1}$
2018_an15	0	0.0057	0	1.685	32.1684	0.8822	63.7386	98.4799	$Zn_{0.98}Sb_{0.01}S_{1.01}$
KMZ_an1	0	0.0115	0.01	2.5884	31.6988	0.7254	61.8225	96.8566	$Zn_{0.97}Sb_{0.02}S_{1.01}$
KMZ_an2	0	0.0142	0.0601	2.6813	32.2032	0.6121	62.1113	97.6822	$Zn_{0.96}Sb_{0.02}S_{1.01}$
KMZ_an3	0	0.0379	0.1227	2.5596	31.3526	0.8513	60.3013	95.2254	$Zn_{0.96}Sb_{0.02}S_{1.02}$
KMZ_an4	0	0.0081	0.022	1.409	32.0244	0.8022	62.0654	96.3311	$Zn_{0.97}Sb_{0.01}S_{1.02}$
KMZ_an5	0	0.013	0	1.7448	31.9473	0.8585	63.3473	97.9109	$Zn_{0.98}Sb_{0.01}S_{1.}$
KMZ_an5	0	0.013	0	1.7448	31.9473	0.8585	63.3473	97.9109	$Zn_{0.98}Sb_{0.01}S_{1}$

The correlations between Zn and Sb are strongly negative so that the increase of the Zn content is correlated with the decrease of Sb content (Table 3). This proves that the deposition of these two elements is done from the same hydrothermal solutions. The correlation of Zn with Fe and Pb have little statistical significance, which shows that Fe and Pb had variable contents in the hydrothermal solutions present during colloform sphalerite crystallization. The presence of obvious quantities of lead in the colloform sphalerite indicates that the fluids from which the depositions were made were intermittently supersaturated. So, we suggest that it is possible that Zn and Sb have the same source, and the other detected elements have another, intermittent source. The correlation between Zn and Bi has little significance, but it is possible for hydrothermal solutions to contain small amounts of bismuth. Bismuth and copper appear in very small quantities and may be present under the form of mechanical impurity in sphalerite.

Table 3. Cross-correlation matrix between the elements identified during microprobe analysis. The statistically significant ($p < 0.05$) correlations are marked with bold letters.

Element	Fe	Bi	Sb	Pb	Zn
Fe	1				
Bi	0.254121	1			
Sb	−0.10204	0.355393	1		
Pb	−0.26614	−0.18413	0.086813	1	
Zn	0.218825	**−0.32911**	**−0.85962**	−0.26285	1

5. Discussion

Valentinite and other antimony oxides ("stibiconite", cervantite, senarmontite) are generally considered secondary minerals formed under oxygenated conditions by oxidation of stibnite, [65]. At the Dealul Crucii and Baia Sprie, it was identified in association with primary minerals calcite, sphalerite, chalcopyrite, and tetrahedrite, without the presence of stibnite. It occurs in the form of idiomorphic crystals deposited on calcite that would indicate a primary mineral and not a secondary mineral deposited on stibnite. It is known that valentinite is deposited from aqueous solutions $Sb(OH)_3$.

A review of the thermodynamic properties of valentinite at hydrothermal conditions is done by Zotov et al. (2003) [66] with a comprehensive discussion about its solubility. According to data found in this article, the concentration of H_2S was low and probably also buffered by the identified sulphides, so that Sb could be transported mainly as $Sb(OH)_3$. The pH range could have been in the wide domain of 2–10, while the temperatures between 100–200 °C. On the other hand, we can conclude that it formed at the end of the hydrothermal process when sulfur fugacity (fS_2) was reduced, fO_2 begins to manifest strongly, and when fluid temperatures decreased through fluid mixing. These conditions for the formation of valentinite were also demonstrated by Biver and Shotyk (2013) [67] who obtained it by hydrothermal processes at a temperature of about 100 °C.

Colloform sphalerite is always associated with low temperature (<100 °C) deposition conditions [11]. According to Barrie et al. (2009) [11], it can be formed by mixing two types of fluids (e.g., bacterial sulfur fluids and hydrothermal fluids). According to Henjes-Kunst (2017) [20], mixing liquids containing, on the one hand, sulphur, originating from various sources, with zinc-rich hydrothermal fluids, on the other hand, would be one major premise for colloform sphalerite deposition. It is very unlikely that in the hydrothermal mineralization from Baia Sprie bacterial sulfur existed, but it is possible that it existed in the surface waters infiltrated in the upper part of the hydrothermal systems, so that the final temperatures of the hydrothermal processes from Baia Sprie could have been between 100–200 °C with a low fO_2 [43]. This theory is also supported by data presented by Manilici et al. (1965) [39] and Buzatu et al. (2015) [26], who demonstrated that stibnite was deposited in the final phases of the hydrothermal process, at temperatures below 200 °C [43]. Colloform sphalerite was subsequently deposited on stibnite and quartz which were already crystallized. Pfaff et al. (2010) [19] consider that the formation of colloform sphalerite is caused by a significant drop in temperature, which could have been in the domain from below 100 °C to at least 150 °C.

On the other hand, determination of the deposition temperature of sphalerite was tried by quantifying the iron content of the sphalerite sample. In his experimental determinations, Kullerrud (1953) [68] proposed the use of the solvus curve in mixed (Zn,Fe)S-FeS crystals applied to the sphalerite-pyrrhotite associations. The first impediment in applying this method in our case is that the Baia Sprie colloform sphalerite cannot be found in this paragenesis. But, using the above mentioned solvus curve and the iron content of the samples, we can obtain a deposition temperature around 100–150 °C. Kellerrud's research could not be confirmed by Barton and Toulmin (1966) [69], respectively by Borman (1967) [70], because for sphalerite in equilibrium with pyrrhotite and pyrite, the amount of FeS increases with a decreasing temperature from 742 °C down to 550 °C, continued by a constant plateau of 20.8% mol FeS down to 303 °C. The subsequent studies of Chernyshev and Anfilogov (1968) [71] and Einaudi (1968) [72] suggest values of FeS in sphalerite of 26% ± 3% mol, respectively, 32.2% ± 1.2% mol, at 300 °C. Moreover, in the temperature domain 300–600 °C, which is of more interest in the metallogenic processes, the FeS content is pressure-dependent. Scott and Barnes (1971) [73], Scot (1973) [74], and Hutchinson and Scott (1981) [75] discussed the possibility of using sphalerite as a geobarometer, not as a geothermometer. This is why the temperatures estimated from the FeS content of sphalerite has to be taken with precaution.

It is possible that these temperatures were reached at Baia Sprie because of the surface water, which contained biogenic sulfur and organic matter, favouring this way, the formation of colloform sphalerite. The examined samples also indicate the existence of a geode that would have allowed the mixing of the surface water with hydrothermal fluids. Hydrothermal fluids would have periodically provided metals that over-saturated the fluids with zinc, and the first mixture with hot water would have formed colloform sphalerite. Roedder (1968) [13] suggested that the colloform texture of sphalerite may occur by rapid deposition from a fluid supersaturated in Zn.

Nodules similar to those found in the colloform sphalerite samples from Baia Sprie were obtained by hydrothermal processes at 150–200 °C by Ibupoto et al. (2013) [60] and Yang et al. (2010) [76]. The fact that the colloform sphalerite from Baia Sprie also include these nodular forms confirms that

the formation temperature domain estimated by us in the previous paragraphs is correct. As a theory to explain the formation of these nodular structures, one could resort to fractal growth models using deterministic ones [77] or diffusion limited aggregation type processes [78]. Determining the fractal descriptors of such natural or manmade nano/microscale materials has to be a completely new study using enhanced 3D imaging or small angle scattering techniques applied to single nodules [79,80].

6. Conclusions

Valentinite and colloform sphalerite, from Baia Sprie and Dealul Crucii, respectively, were formed in epithermal conditions at low temperatures (100–150 °C), in association with other minerals formed at these low temperatures.

Chemical analyses and interpretation of the obtained micro-Raman spectra demonstrate the presence of valentinite. The stoichiometric formula of valentinite is close to Me_2O_3. Chemical impurities are present in very small quantities. Tin is most frequently encountered because it can be a substitute for antimony in the valentinite's formula.

The first description of the occurrence of colloform sphalerite and valentinite in hydrothermal and inclusive deposits in the Baia Mare area, which are also associated with the Neogene age, was presented in this article.

The structure with alternate banding on the nano-/micro-scale, identified by the optical microscope, SEM and BES images is typical for colloform sphalerite and suggests a genesis due to episodic precipitation.

The presence of spherical nano-/microscale particles also characterize the colloform sphalerite from Baia Sprie and are similar to those obtained synthetically by hydrothermal processes at low temperatures.

Raman and X-ray diffraction analysis demonstrates the presence of pure sphalerite with low iron content.

Microprobe analyses made on these colloform sphalerite samples also certify the presence of sphalerite with low iron content but with antimony and lead impurities that replace the positions of zinc.

The stoichiometric formula of colloform sphalerite is close to ZnS.

Author Contributions: Conceptualization, G.D.; methodology, G.D., A.B., I.A.A., D.B.; software, A.B., I.A.A., Z.L.S.; validation, G.D., A.B. and I.A.A.; formal analysis, G.D., A.B., I.A.A., Z.L.S., G.I., D.B.; investigation, G.D., A.B., I.A.A.; resources, G.D., A.B., I.A.A.; data curation, I.D.; writing—original draft preparation, G.D., A.B., I.A.A.; writing—review and editing, G.D., A.B., I.A.A., Z.L.S.; visualization, A.B., I.A.A.; supervision, Z.L.S.; project administration, G.D. All authors have read and agreed to the published version of the manuscript.

Funding: This research received no external funding.

Acknowledgments: The authors are grateful to the County Museum of Mineralogy, "Victor Gorduza", Baia Mare (Romania) for providing the samples. Thanks are also due to the staff of State Geological Institute of Dionýz Štúr (Bratislava, Slovakia) and to the Geological Institute of Romania (Bucharest, Romania). We extend our gratitude to the anonymous reviewers for their time spent reading the manuscript and for the valuable suggestions, as well as to the assistant editor for the editorial handling of the manuscript.

Conflicts of Interest: The authors declare no conflict of interest.

References

1. Iștvan, D.; Halga, S.; Vârșescu, I.; Grancea, L.; Chiuzbăian, C. New data on the upper part of the Baia Sprie deposit, East Carphatians, Romania. *An. Științifice ale Univ. Al. I. Cuza Iași Geol.* **1996**, *XLII-supliment*, 101–110.
2. Krenner, J. Andorit uj hazai ezustercz. *Mathem es trem. tud. Estesito.* **1893**, *11*, 119–122.
3. Krenner, J. Egy Felsöbányántatált uj olomerc. *Akad. Értek.* **1881**, *15*, 111–118.
4. Kenngott, A. Mineralogische Notizen, Sitzungsberichte der Akad. *Der Wiss. Wien.* **1853**, *10*, 288–299.
5. Zsivny, V. Klebelsbergit, egy új ásvány Felsöbányáról. *Math. t.-t. Ért.* **1929**, *24*, 19–24.
6. Schroeckinger, J. Dietriechit, ein neuer Alaun aus Ungarn. *Verhandl. Geol. Bundesanst. Wien.* **1878**, 189–191.

7. Schroeckinger, J. Sphärosiderite von schr hohen Mangangehalte aus ungarn, II. Szikit, ein neues Mangansulphat. *Geol. Reichsanst. Wien Verhandl.* **1877**, *1877*, 115–117.
8. Finalyi, I.; Koch, S. Fülöppite, a new Hungarian Mineral of the plagionite-semseyite group. *Min. Mag.* **1929**, *22*, 179–189.
9. Krenner, J.; Loczka, J. Fizélyit, ein neues ungarisches Silberez. *Math. t.-t. Ért.* **1923**, *40*, 18–21.
10. Svensson, C. The crystal structure of orthorhombic antimony trioxide, Sb_2O_3. *Acta Crystallogr.* **1974**, *B30*, 458–461. [CrossRef]
11. Barrie, C.D.; Boyce, A.J.; Boyle, A.P.; Williams, P.J.; Blake, K.; Wilkinson, J.J.; Lowther, M.; McDermott, P.; Prior, D.J. On the growth of colloform textures: A case study of sphalerite from the Galmoy ore body, Ireland. *J. Geol. Soc. Lond.* **2009**, *166*, 563–582. [CrossRef]
12. Rogers, A.F. A review of the amorphous minerals. *Geology* **1917**, *25*, 515–541. [CrossRef]
13. Roedder, E. The noncolloidal origin of "colloform" textures in sphalerite ores. *Econ. Geol.* **1968**, *63*, 45l–471. [CrossRef]
14. Fowler, A.D.; L'Heureux, I. Self-organized banded sphalerite and branching galena in the Pine Point ore deposit, Northwest Territories. *Can. Mineral.* **1996**, *34*, 1211–1222.
15. Pfaff, K.; Koenig, A.; Wenzel, T.; Ridley, I.; Hildebrandt, H.L.; Leach, L.D.; Markl, G. Trace and minor element variations and sulfur isotopes in crystalline and colloform ZnS: Incorporation mechanisms and implications for their genesis. *Chem. Geol.* **2011**, *286*, 118–134. [CrossRef]
16. Heyl, A.V.; Agnew, A.F.; Lyons, E.J.; Behre, C.H., Jr. The geology of the upper Mississippi Valley zinc lead district. *U.S. Ecol. Surv. Prof. Paper.* **1959**, *309*, 310.
17. McLimans, R.K.; Barnes, H.L.; Ohmoto, H. Sphalerite stratigraphy of the upper Mississippi Valley lead-zinc district, southwes Wtisconsin. *Econ. Geol.* **1980**, *75*, 351–361. [CrossRef]
18. Lasmanis, R. Galena: From Mississippi Valley-Type Deposits. *Rocks Miner.* **1989**, *64*, 11–34. [CrossRef]
19. Pfaff, K.; Hildebrandt, L.H.; Leach, D.L.; Jacob, D.E.; Markl, G. Formation of the Wiesloch Mississippi Valley-type Zn-Pb-Ag deposit in the extensional setting of the Upper Rhinegraben, SW Germany. *Miner. Depos.* **2010**, *45*, 647–666. [CrossRef]
20. Henjes-Kunst, E.; Raith, G.J.; Boyce, J.A. Micro-scale sulfur isotope and chemical variations in sphalerite from the Bleiberg Pb-Zn deposit, Eastern Alps, Austria. *Ore Geol. Rev.* **2017**, *90*, 52–62. [CrossRef]
21. Csontos, L. Tertiary tectonic evolution of the intra-Carpathian area: A review. *Acta Vulcanol.* **1995**, *7*, 1–13.
22. Neubauer, F.; Lips, A.; Kouzmanov, K.; Lexa, J.; Ivășcanu, P. Subduction, slab detachmentand mineralization: The Neogene in the Apuseni Mountains and Carpathians. *Ore Geol. Rev.* **2005**, *27*, 13–44. [CrossRef]
23. Seghedi, I.; Downes, H.; Szakács, A.; Mason, P.; Thirwall, M.T.; Roșu, E.; Pécskay, Z.; Márton, E.; Panaiotu, C. Neogene–Quaternary magmatism and geodynamics in the Carpathian–Pannonian region: A synthesis. *Lithos* **2004**, *72*, 117–146. [CrossRef]
24. Seghedi, I.; Downes, H. Geochemistry and tectonic development of Cenozoic magmatism in the Carpathian–Pannonian region. *Gondwana Res.* **2011**, *20*, 655–672. [CrossRef]
25. Nedelcu, L.; Bălașa, E.; Roșu, N.; Bordea, R. Consideratii Noi asupra zăcământului Dealul Crucii pe baza rezultatelor unor foraje recente. *Comptes Rendus des Séances, (1967-1968), 2. Zăcăminte.* **1970**, *Tomes LV*, 47–66.
26. Buzatu, A.; Damian, G.; Dill, G.H.; Buzgar, N.; Apopei, I.A. Mineralogy and geochemistry of sulfosalts from Baia Sprie ore deposit (Romania)—New bismuth minerals occurrence. *Ore Geol. Rev.* **2015**, *65*, 132–147. [CrossRef]
27. Giușcă, D.; Barcoş, M.; Lang, B.; Stan, N. Neogene volcanism and metallogenesis in the Gutâi Mountains. In *Guidebook 12, Symposium on Volcanism and Metallogenesis*; Geological Institute of Romania: Bucharest, Romania, 1973; 50p.
28. Szakács, A.; Pécskay, Z.; Silye, L.; Balogh, K.; Vlad, D.; Fülöp, A. On the age of the Dej Tuff, Transylvanian Basin (Romania). *Geol. Carpathica.* **2012**, *63*, 139–148. [CrossRef]
29. Borcoş, M.; Lang, B.; Peltz, S.; Stan, N. Volcanisme neogene des Monts Gutâi. *Geol. Geogr. Geoph. Ser. Geologie.* **1973**, *17*, 1.
30. Edelstein, O.; Bernard, A.; Kovacs, M.; Crihan, M.; Pecskay, Z. Preliminary date regarding the K-Ar ages of some eruptive rocks from Baia Mare Neogene volcanic zone. *Rev. Roum. de Geol.* **1992**, *36*, 45–60.
31. Damian, F.; Damian, G.; Constantina, C. The Subvulcanic Magmatic Rocks from the Nistru Zone (Gutii Mountains). *Carpathian J. Earth Environ. Sci.* **2009**, *4*, 101–122.

32. Popescu, C.G. A geodinamic Model regarding the Neogene Volcanism and the associated Metallogenetic District (The East Carpathians). *An. Univ. Bucureşti Serie Geologie* **1994**, *XLIII*, 19–26.
33. Lang, B.; Edelstein, O.; Steinitz, O.; Kovacs, M.; Halga, S. Ar–Ar dating of adularia—A tool in understanding genetic relations between volcanism and mineralization: Baia Mare area (Gutîi Mountains), Northwestern Romania. *Econ. Geol.* **1994**, *89*, 174–180. [CrossRef]
34. Damian, G.; Damian, F.; Iștvan, D. The Neogene metallogenesis of the central western area of the Baia Mare District (Gutâi Mts – East Carpathians). In *the Volum Abstract a Final GEODE-ABCD Workshop, Geodynamics and Ore Deposit Evolution of the Alpine-Balkan- Carpathian-Dinaride Province, Seggauberg*; University of Salzburg: Salzburg, Austria, 2003; p. 26.
35. Popescu, C.G.; Ștefănoiu, A. Specific features and perspectives of Baia Sprie deposit. *Revista Minelor.* **1972**, *23*, 326–329. (In Romanian)
36. Borcoș, M.; Vlad, S.; Udubașa, G.; Găbudeanu, B. Qualitative and quantitative metallogenetic analysis of the ore genetic units in Romania. *Rom. J. Miner. Depos.* **1998**, *78*, 1–160.
37. Popescu, C.G. *Metalogenie aplicată şi prognoza geologică partea a II-a*; Universităţii Bucureşti: Bucharest, Romania, 1986; p. 210. (In Romanian)
38. Damian, F. The mineralogical characteristics and the zoning of the hydrothermal types alteration from Nistru ore deposit, Baia Mare Metallogenetic district. *Studia Univ. Babeş-Bolyai Geol.* **2003**, *XLVIII*, 101–112. [CrossRef]
39. Manilici, V.; Giușcă, D.; Stiopol, V. Study of Baia Sprie ore deposit. *Mem. Com. Geol. Inst. Geol. Bucur.* **1965**, *VII*, 1–95. (In Romanian)
40. Ghitulescu, T.P. Distribution de la mineralizations dans les gissements d'âge tertiaires de Transilvanie. *Bul. Soc. Rom. de Geol.* **1932**, *II*, 56–97.
41. Udubaşa, G.; Ilinca, G.; Marincea, Ş.; Săbău, G.; Rădan, S. Minerals in Romania: The State of the Art 1991. *Rom. J. Mineral.* **1992**, *75*, 1–51.
42. Măldărascu, I.; Popescu, C.G. Physical and structural control of hydrothermaldeposits formation from the eastern part of Baia Mare metallogenetic district. *Stud. Cercet. Geol. Geofiz. Geogr.* **1981**, *26*, 241–248. (In Romanian)
43. Borcoș, M.; Lang, B.; Boștinescu, S.; Gheorghita, I. Neogene hydrothermal ore deposits in the volcanic Gutâi Mountains. III. Dealul Crucii–Băiu district. A. Herja, Baia Sprie and uior ore deposits. *Rev. Roum. Géol. Geophys. Ser. Géol.* **1975**, *19*, 21–35.
44. Marias, F. *Metallogeny of the Baia Mare Mining District—An Approach on the Cavnic Hydrothermal System*; Cornelius Ed.: Glendale Heights, IL, USA, 2005; p. 378. (In Romanian)
45. Popescu, C.G.; Neacșu, A. *Metalogenie aplicată și prognoză geologică*; Ed. Univ. București: Bucharest, Romania, 2009; p. 209. (In Romanian)
46. Damian, G.; Nedelcu, L.; Iștvan, D. Hydrothermal ore deposits at Baia Sprie and Turt, in Excursion guides, Ghe. Udubasa ed., Mineral and mineral occurrences in the Baia Mare mining district. *Rom. J. Mineral.* **1995**, *77*, 45–63.
47. Stanciu, C. Hydrothermal transformation processes in Herja and Baia Sprie ore deposits—Gutîi Mountains. *Inst. Geol. Stud. Teh. si Econ. Seria I.* **1973**, *9*, 73–94. (In Romanian)
48. Damian, G.; Damian, F.; Cook, J.N.; Ciobanu, L.C. Ag-sulphosalts in upper parts of the Baia Mare district (Romania): Microanalyses and implications for the deposit zonality. In Proceedings of the Proceedings and abstracts of the 6th International Symposium on Mineralogy, Cluj-Napoca, Romania, 18–21 September 2003; pp. 37–39.
49. Petrulian, N.; Steclaci, L. Studiul mineralogic și geochimic al Filonului Nou de la Baia Sprie. *Stud. Cerc. Geologie.* **1971**, *XVI*, 294–320.
50. Superceanu, C. Contribuții la paragenezele scheelitului și wolframitului din zăcământul de minereuri complexe de la Baia Sprie. *Rev. Min.* **1957**, *8*, 399–404.
51. Buzatu, A.; Damian, G.; Buzgar, N. Raman and infrared studies of weathering products from Baia Sprie ore deposit (Romania). *Rom. J. Miner. Depos.* **2012**, *85*, 7–10.
52. Buzatu, A.; Buzgar, N.; Damian, G.; Vasilache, V.; Apopei, A.I. The determination of the Fe content in natural sphalerites by means of Raman spectroscopy. *Vib. Spectrosc.* **2013**, *68*, 220–224. [CrossRef]
53. Koch, A.I. Valentinit und orientiert weitengewachsene Baryte von Felsobanya, Steinslaz von Deesakna F.K. *Ref. N. Jb. Min.* **1926**, *53*, 81–84.

54. Tokody, L. Felsobanya asvanyai geokemiai Szempontbol. *Math. T.-t Ert.* **1942**, *61*, 191–223.
55. Schaller, W.T. Crystallography of valentinite (Sb_2O_3) and andorite (?) ($2PbS–Ag_2S–3Sb_2S_3$) from Oregon. *Am. Mineral.* **1937**, *22*, 651–666.
56. Palache, C.; Berman, H.; Frondel, C. *The System of Mineralogy of James Dwight Dana and Edward Salisbury Dana Yale University 1837-1892, Volume I: Elements, Sulfides, Sulfosalts, Oxides*; John Wiley and Sons, Inc.: New York, NY, USA, 1944; pp. 547–550.
57. Mestl, G.; Ruiz, P.; Delmon, B.; Knozinger, H. Sb_2O_3/Sb_2O_4 in reducing/oxidizing environments: An in situ Raman spectroscopy study. *J. Phys. Chem.* **1994**, *98*, 11276–11282. [CrossRef]
58. Orman, R.G. Phase Transitions in Antimony Oxides and Related Glasses. Master's Thesis, University of Warwick, Coventry, UK, 2005.
59. Geng, A.; Cao, L.; Wan, C.; Ma, Y. High-pressure Raman investigation of the semiconductor antimony oxide. *Phys. Status Solidi. C* **2011**, *8*, 1708–1711. [CrossRef]
60. Ibupoto, Z.H.; Khun, K.; Liu, V.; Willander, M. Hydrothermal Synthesis of Nanoclusters of ZnS Comprised on Nanowires. *Nanomaterials* **2013**, *3*, 564–571. [CrossRef] [PubMed]
61. ASTM. *American Society for Testing and Materials: Powder Difraction File, Alphabetical Index (Chemical and Mineral Name*; Int. Cent. Difraction Data: Swarthmore, PA, USA, 1987; p. 664.
62. Kharbish, S. A Raman spectroscopic investigation of Fe-rich sphalerite: Effect of Fe-substitution. *Phys. Chem. Miner.* **2007**, *34*, 551–558. [CrossRef]
63. Osadchii, E.G.; Gorbaty, Y.E. Raman spectra and unit cell parameters of sphalerite solid solutions (FexZn1-xS). *Geochim. Cosmochim. Acta.* **2010**, *74*, 568–573. [CrossRef]
64. Plotinskaya, O.Y.; Prokofiev, V.Y.; Damian, G.; Damian, F.; Lehmann, B. Tthe Cisma Deposit, Baiut District, Eastern Carpathians, Romania: Sphalerite composition and formation conditions. *Carpathian J. Earth Environ. Sci.* **2012**, *7*, 265–273.
65. Mason, B.; Vitalian, C. The mineralogy of the antimony oxides and antimonates. *Mineral. Mag. J. Mineral. Soc.* **1953**, *30*, 100–112. [CrossRef]
66. Zotov, A.V.; Shikina, N.D.; Akinfiev, N.N. Thermodynamic properties of the Sb(III) hydroxide complex $Sb(OH)_3(aq)$ at hydrothermal conditions. *Geochim. Cosmochim. Acta* **2003**, *67*, 1821–1836. [CrossRef]
67. Biver, M.; Shotyk, W. Stibiconite (Sb_3O_6OH), senarmontite (Sb_2O_3) and valentinite (Sb_2O_3): Dissolution rates at pH 2–11 and isoelectric points. *Geochim. Cosmochim. Acta* **2013**, *109*, 268–279. [CrossRef]
68. Kullerrud, G. The FeS-ZnS system, a geological thermometer, Narsk. *Geol. Tidsskr.* **1953**, *22*, 61–147.
69. Barton, P.B.; Toulmin, P. Phase relations involving sphalerite in the Fe-Zn-S system. *Econ. Geol.* **1966**, *61*, 815–849. [CrossRef]
70. Boorman, R.S. Subsolidus studies in the ZnS-FeS-FeS_2 system. *Econ. Geol.* **1967**, *62*, 614–631. [CrossRef]
71. Chernyshev, L.V.; Anfilogov, V.N. Subsolidus phase relations in the ZnS-FeS-FeS_2 system. *Econ. Geol.* **1968**, *63*, 841–843. [CrossRef]
72. Einaudi, T.M. Spalerite-Pyrhotite-Pyrite Equilibria a Revoluation. *Econ. Geol.* **1968**, *63*, 832–834. [CrossRef]
73. Scott, S.D.; Barnes, H.L. Sphalerite Geothermometry and Geobarometry. *Econ. Geol.* **1971**, *66*, 653–669. [CrossRef]
74. Scot, S.D. Experimental calibration of the sphalerite geobarometer. *Econ. Geol.* **1973**, *68*, 466–474. [CrossRef]
75. Hutchinson, N.M.; Scott, S.D. Sphalerite geobarometry in the Cu-Fe-Zn-S system. *Econ. Geol.* **1981**, *76*, 143–156. [CrossRef]
76. Yang, Z.X.; Zhong, W.; Deng, Y.; Au, C.; Du, Y.W. Fabrication and Optical Behaviors of Core–Shell ZnS Nanostructures. *Nanoscale Res. Lett.* **2010**, *5*, 1124–1127. [CrossRef]
77. Vicsek, T.M. Deterministic models of fractal and multifractal growth. *Physica D* **1989**, *38*, 356–361. [CrossRef]
78. Witten, T.A., Jr.; Sander, L.M. Diffusion-Limited Aggregation, a Kinetic Critical Phenomenon. *Phys. Rev. Lett.* **1981**, *47*, 1400–1403. [CrossRef]
79. Anitas, E.M. Small-Angle Scattering from Weakly Correlated Nanoscale Mass Fractal Aggregates. *Nanomaterials* **2019**, *9*, 648. [CrossRef]
80. Anitas, E.M.; Marcelli, G.; Szakacs, Z.; Todoran, R.; Todoran, D. Structural Properties of Vicsek-like Deterministic Multifractals. *Symmetry* **2019**, *11*, 806. [CrossRef]